Determination of time-reversal symmetry breaking lengths in an InGaAs interferometer array

S L Ren[1]**, J J Heremans**[1]**, S Vijeyaragunathan**[2]**, T D Mishima**[2]
and M B Santos[2]

[1] Department of Physics, Virginia Tech, Blacksburg, VA 24061, USA
[2] Homer L. Dodge Department of Physics and Astronomy, University of Oklahoma, Norman, OK 73019, USA

E-mail: heremans@vt.edu

CrossMark

Abstract

Quantum interference oscillations due to the Aharonov–Bohm phase were measured in a ring interferometer array fabricated on a two-dimensional electron system in an InGaAs/InAlAs heterostructure. Coexisting oscillations with magnetic flux periodicity h/e and $h/2e$ were observed and their amplitudes compared as function of applied magnetic field. The $h/2e$ oscillations originate in time-reversed trajectories with the ring interferometers operating in Sagnac-type mode, while the h/e oscillations result from Mach–Zehnder operation. The $h/2e$ oscillations require time-reversal symmetry and hence can be used to quantify time-reversal symmetry breaking, more particularly the fundamental mesoscopic dephasing length associated with time-reversal symmetry breaking under applied magnetic field, an effective magnetic length. The oscillation amplitudes were investigated over magnetic fields spanning 2.2 T, using Fourier transforms over short segments of 40 mT. As the magnetic field increased, the $h/2e$ oscillation amplitude decreased due to time-reversal symmetry breaking by the local magnetic flux in the interferometer arms. A dephasing model for quantum-coherent arrays was used to experimentally quantify effective magnetic lengths. The data was then compared with analytical expressions for diffusive, ballistic and confined systems.

Keywords: Aharonov–Bohm effect, quantum coherent transport, InGaAs heterostructures, time-reversal symmetry

(Some figures may appear in colour only in the online journal)

1. Introduction

Quantum dephasing in mesoscopic systems can be experimentally studied via the Aharonov–Bohm (AB) oscillations in the electrical conductance of an interferometer structure versus applied magnetic field B. AB oscillations arise from quantum interference between partial waves on trajectories in spatially separate interferometer arms when inserting a magnetic flux ϕ between the two arms (for reviews, see [1–4]). When the spatially separated trajectories enclose a magnetic flux quantum h/e (where $h = 2\pi\hbar$ with $\hbar$ the Planck constant and e the electron charge), a relative AB phase of 2π is accumulated between

the partial waves [2], resulting in oscillations in transmittance and conductance with periodicity h/e (figure 1(a)). The oscillations result from minimal coupling of the particle charge to the magnetic vector potential and are evidence of the non-local quantum nature of mesoscopic conductance phenomena. The interferometric setup described above, yielding a periodicity of h/e due to the AB phase, is a Mach–Zehnder (MZ) interferometer and can be nanolithographically fabricated in solid-state systems as an AB ring as depicted in figure 1(a). In a single MZ interferometer the spatial asymmetry between the two arms, originating in fabrication and materials imperfections, can give rise to an additional phase shift between two
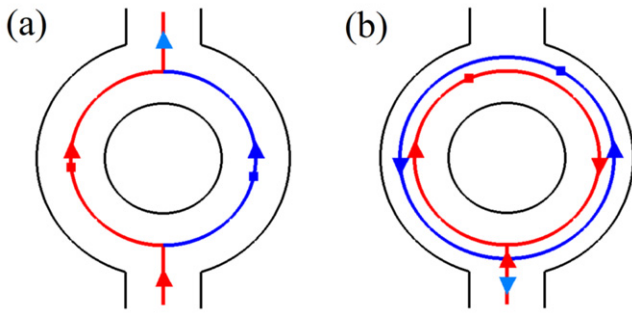
Figure 1. (*a*) Mach–Zehnder (MZ) interferometer, based on trajectories in spatially separate arms. (*b*) Sagnac-type (ST) interferometer, based on exact time-reversed trajectories (for clarity, trajectories are shown spatially non-overlapping).

partial waves if each samples only one arm [4–6]. Hence if a finite number of MZ interferometers are concatenated, ensemble averaging will diminish the measured conductance oscillation amplitude [7–12]. Yet, trajectories through the interferometer arms exist which are immune to such spatial asymmetry, namely exact time-reversed trajectories which probe both interferometers arms in a time-reversed scattering sequence (figure 1(*b*)). Via the AB phase the time-reversed trajectories give rise to Altshuler–Aronov–Spivak (AAS) conductance oscillations and these survive ensemble averaging over a network of interferometers [4, 7, 13–16]. Interference phenomena relying on time-reversed trajectories are typical of Sagnac-type (ST) interferometers (figure 1(*b*)). The AAS oscillations, induced by the AB phase but relying on time-reversal symmetry, appear with a periodicity in ϕ of $h/2e$ since they enclose the flux twice. In the same mesoscopic ring geometries (figure 1), the AB phase thus induces both MZ interferometric oscillations relying on spatial symmetry and with periodicity h/e and ST interferometric oscillations, which we for this work define as relying on time-reversal symmetry and showing periodicity $h/2e$ (AAS oscillations). In large arrays of interferometers, ensemble averaging and spatial asymmetry will lead to dominance of the $h/2e$ AAS oscillations over the MZ oscillations. Yet AAS oscillations require time-reversal symmetry, broken by B. If magnetic flux penetrates the interferometer arms (which we will refer to as local ϕ), rather than only the space between interferometer arms (non-local ϕ), then time-reversal symmetry in the arms will be broken and the AAS oscillation amplitude will decay [4, 8, 13, 16–18]. Typical experiments are performed by applying a uniform B, resulting in both local and non-local ϕ and hence an AAS amplitude diminishing with $|B|$ is observed. This decay of the AAS quantum interference phenomenon is akin to the disappearance of the quantum corrections of weak-localization and anti-localization with increasing $|B|$. In contrast MZ oscillations relying on spatial symmetry, nominally survive to high B. In MZ interference, rather than a decay of the amplitude, a modulation of the amplitude approximately periodic in the local ϕ is observed [19].

At low temperatures T in solid-state systems, other causes also contribute to reduction of oscillation amplitudes, such as decoherence by fluctuations in the electromagnetic background (Nyquist decoherence) [18, 20–22], by particle leakage from the quantum system (dwell-time-limited

decoherence) [18, 23] and by energy smearing from excitation exceeding the Thouless energy [19]. These mechanisms lead to irreversible dephasing, referred to as decoherence [24] and determine the phase coherence length L_ϕ, defined as the distance electrons travel before their quantum phase is randomized by inelastic scattering processes. The characteristic length over which time-reversed partial waves dephase in B due to the accumulated AB phase is a magnetic length L_B, which can be estimated from the quantum interference effects of the AB phase. In an unconfined system, a closed trajectory will accumulate a unity quantum phase if the trajectory encloses a magnetic flux $\hbar/e$. Defining the area enclosed by the trajectory as L_B^2, we find $L_B = l_m \equiv \sqrt{\hbar/(eB)}$. L_B is the characteristic length for breaking of time-reversal symmetry and enters in expressions of decoherence analogously to L_ϕ. The corresponding decoherence and dephasing rates (inverse times) can be added according to Matthiessen's rule [17, 25, 26]. In a diffusive approach, L_ϕ and L_B are related to the phase coherence time τ_ϕ and magnetic dephasing time τ_B respectively by $L_{\phi,B} = \sqrt{D\tau_{\phi,B}}$, where D is the diffusion coefficient. The effective coherence length L_C combining both effects hence is obtained as

$$L_C = \left(L_\phi^{-2} + L_B^{-2}\right)^{-\frac{1}{2}} \tag{1}$$

The expression $L_B = \sqrt{\hbar/(eB)}$ only applies to unconfined systems and equation (1) supposes diffusive transport. Expressions for L_B have been derived extending the range of applicability to confined [25] and ballistic [27, 28] systems, as explained below. Yet, hitherto the expressions have not been put to a direct comparative experimental test. The work below demonstrates the applicability of the expressions for L_B to quantum transport at low T by using an array of mesoscopic interferometers in ST mode, sensitive to time-reversal symmetry breaking. The array is fabricated on a high-mobility InGaAs/InAlAs heterostructure and magnetotransport through the array is measured at fixed $T = 0.4$ K, revealing AAS oscillations. A strong correlation between the Fourier amplitude of the AAS oscillations and a length L_B is observed. By fitting the Fourier amplitude of AAS oscillations, we experimentally derive values for the mesoscopic time-reversal symmetry breaking length L_B as function of B. The work further shows that MZ interference due to the AB phase, also observed in the interferometer array, is insensitive to time-reversal symmetry breaking. Due to spin–orbit interaction in the InGaAs/InAlAs heterostructure, a weak anti-localization (WAL) [14, 22, 26, 29, 30] background in the magnetotransport is also observed, further discussed below.

2. Experiments

The device consists of a 5×5 AB ring array, fabricated on an In$_{0.64}$Ga$_{0.36}$As/In$_{0.45}$Al$_{0.55}$As heterostructure using electron-beam lithography and inductively coupled plasma reactive ion etching (ICP-RIE). Figure 2(*a*) shows a scanning electron micrograph of the ring array, with 5 parallel necklaces each of 5 series-connected rings. The classical resistance of the array is thus equivalent to one ring. The heterostructure
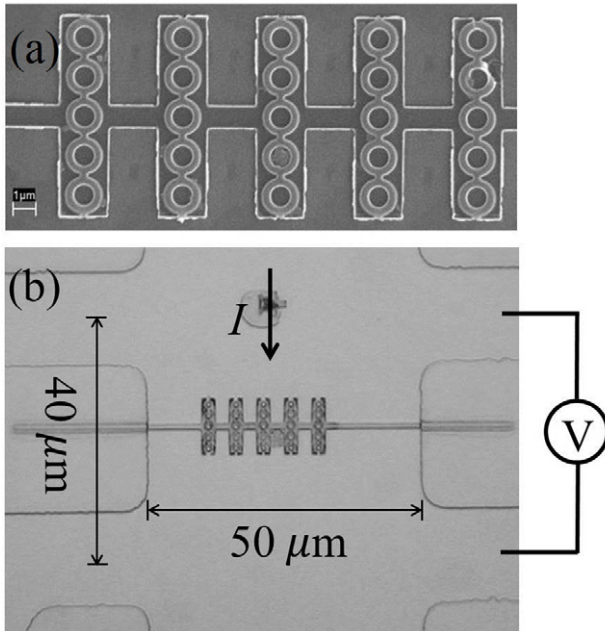
Figure 2. (*a*) Micrograph of a representative 5×5 ring array. Each ring has average radius 650 nm and lithographic arm width 300 nm. The separation between columns is 2.2 μm. (*b*) Schematic four-terminal measurement setup.

contains a two-dimensional electron system (2DES) in a 10 nm wide $\mathrm{In}_{0.64}\mathrm{Ga}_{0.36}\mathrm{As}$ quantum well located 50 nm beneath the surface. The 2DES has areal density $N_S = 1.1 \times 10^{12}$ cm^{-2} calculated from Hall coefficient, yielding a Fermi wavelength $\lambda_\mathrm{F} = 24$ nm, has resistivity $\rho_{2D} = 121$ $\Omega/\square$ at 0.4 K and mobility $\mu = 4.7 \times 10^4$ cm^2 (Vs)$^{-1}$. The 2DES state was modified by illuminating with an LED at low T, increasing N_S while lowering μ. While the transport properties vary between cooldowns, for the present experiments the resistance R of ring array is 3400 Ω, within 5% variability. The lithographic width of each ring arm is 300 nm and the rings have average radius $r = 650$ nm (the central antidot has radius 500 nm). Due to a depletion layer, the effective conducting width w of each arm will be smaller than 300 nm. The conducting width w can be estimated at $w \simeq 100$ nm from R and the resistance of structures peripheral to the array. The number of transport channels due to transverse quantization can be estimated as $2w/\lambda_\mathrm{F} \approx 8$. The separate transport channels are expected to maintain the same phase for AAS oscillations, since their average locations in the interferometer arms coincide and since channel-dependent scattering phenomena leading to spatial asymmetry in the rings do not affect AAS oscillations which rely on time-reversal symmetry. Hence the AAS oscillation intensity, of interest in this work, is not expected to be sensitive to the number of transport channels. The mobility mean free path, limited by elastic momentum scattering processes, is defined as $l_\mathrm{e} = v_\mathrm{F}\tau_\mathrm{e}$, where v_F is the Fermi velocity, $\tau_\mathrm{e} = \mu m^* e^{-1}$ is the momentum relaxation time derived from μ and m^* represents the electron effective mass ($0.035 m_\mathrm{e}$ at the Γ-point in our system, with m_e the free-electron mass). Accounting for non-parabolicity of the conduction band, the 2DES has $l_\mathrm{e} = 1.54$ μm. Each ring thus operates in or near the ballistic regime, since l_e
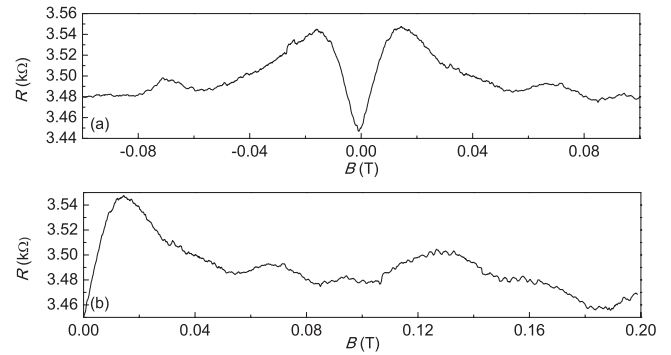

Figure 3. $R(B)$ versus B measured on the array at $T = 0.4$ K over two spans of 0.2 T. AAS and MZ oscillations ride on a magnetoresistance background dominated by WAL at low B. Panel (*a*) focuses on the region -0.1 T $< B < 0.1$ T, while panel (*b*) shifts to $0 < B < 0.2$ T to emphasize the visibility of MZ oscillations.

approximately equals the MZ path length $\pi r = 2.0$ μm and ballistic, rather than diffusive, expressions are appropriate to describe the mesoscopic transport phenomena. From previous measurements in this heterostructure [19], it is estimated that $L_\phi = 3.0$ μm at $T = 0.4$ K.

Magnetotransport through the ring array was measured using standard four-terminal low frequency lock-in techniques (figure 2(*b*)) at $T = 0.4$ K under applied current of 20 nA and recorded as $R(B)$. B was applied normal to the plane of 2DES, varying from -2.3 T to 2.3 T in small step sizes to capture the AAS and MZ oscillations in $R(B)$. Data is depicted in figure 3, as $R(B)$ versus B. At uniformly applied B, the flux threading the ring is $\phi(B) = B\pi r^2$, allowing a prediction from lithographic sizes of the periodicity of $R(B)$ in B. The MZ oscillations (periodicity in non-local ϕ of h/e) have expected periodicity ΔB_MZ in B of 3.1 mT and the AAS oscillations (periodicity in non-local ϕ of $h/2e$) have expected ST periodicity ΔB_ST of 1.56 mT.

3. Results and analysis

As shown in figure 3(*a*), the array yields a strong WAL positive magnetoresistance background, on which interference oscillations ride. Both figures 3(*a*) and (*b*) span 0.2 T, with figure 3(*a*) emphasizing the region $B \sim 0$ and figure 3(*b*) extending the same data to 0.2 T. In figures 3(*a*) and (*b*) strong oscillation signals are observed, as a superposition of AAS ($h/2e$) oscillations at low $B < 5$ mT riding on the strong WAL background and MZ (h/e) oscillations prominent for $B > 20$ mT. Fourier spectra (below) will bear out this identification. The WAL [14, 22, 26, 29, 30] background extends to $B \approx 15$ mT. In the array, WAL is observed to yield a stronger positive magnetoresistance signal than in unconfined macroscopic regions of the same 2DES. The increased magnitude of the WAL magnetoresistance results from the confined geometry, as geometrical factors such as the conducting width of wire-like structures play a role in the magnitude and extent in B of WAL features [15, 31]. For the discussion below, we remove the magnetoresistance background to enhance the visibility of the low-B AAS oscillations. As further examples, figure 4 shows $R(B)$ at
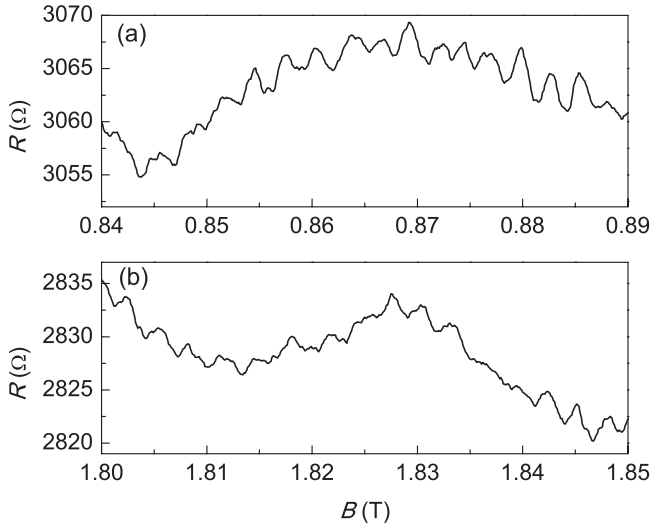
Figure 4. $R(B)$ versus B over two spans of 50 mT, centered on 0.865 T (*a*) and 1.825 T (*b*). Only MZ oscillations (periodicity h/e) are visible at these higher B.
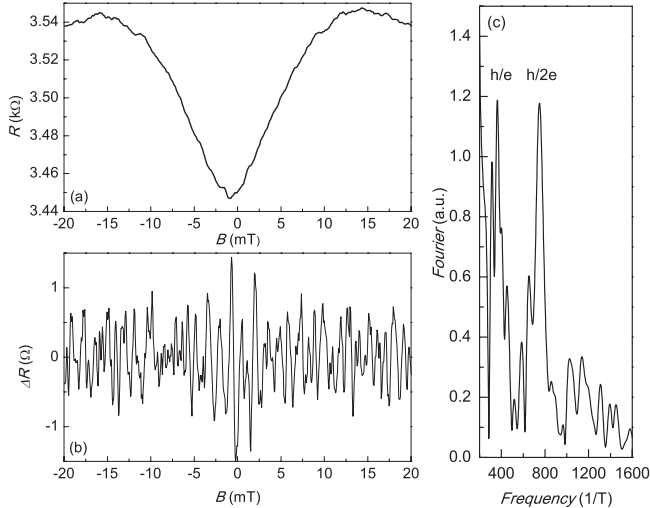

Figure 5. (*a*) $R(B)$ versus B at low B spanning ± 20 mT; (*b*) After removing the WAL magnetoresistance background from (*a*), AAS and MZ oscillations clearly appear. (*c*) Fourier transform of the data in (*a*) with two maxima clearly marked out: the h/e maximum corresponding to MZ oscillations and the $h/2e$ maximum corresponding to AAS oscillations.

higher B in spans of 50 mT, centered on 0.865 T and 1.825 T respectively. The average periodicity of the oscillations in figure 4 is 2.8 mT, demonstrating that the oscillations have periodicity in non-local ϕ of h/e and result from MZ interference. The experimental $\Delta B_{MZ} = 2.8$ mT indeed differs by only 10% from the geometrically expected 3.1 mT. No component in $h/2e$ appears in such higher B spans and ST operation is indeed expected to be suppressed at higher B due to breaking of time-reversal symmetry.

Figure 5(*a*) focuses on $R(B)$ versus B at low B, spanning ± 20 mT. Upon removal of the WAL background in figure 5(*b*), AAS oscillations clearly appear for $B < 5$ mT. The Fourier spectrum corresponding to figure 5(*b*) is contained in figure 5(*c*). In the spectrum, the MZ oscillations

produce a maximum at $1/B = 360 \, \text{T}^{-1}$, corresponding to periodicity $\Delta B_{MZ} = 2.77$ mT and the AAS ST oscillations produce a maximum at $1/B = 750 \, \text{T}^{-1}$, corresponding to periodicity $\Delta B_{ST} = 1.33$ mT. The Fourier transform confirms that $\Delta B_{ST} \approx \frac{1}{2} \Delta B_{MZ}$ and yields values close to geometrical expectations, hence corroborating the existence of MZ h/e and ST $h/2e$ oscillations in the range ± 20 mT.

Figure 6 depicts Fourier spectra illustrating the decay of AAS oscillations with increasing B, caused by time-reversal symmetry breaking and quantitatively described by the shortening of L_B with increasing B in equation (1). The Fourier spectra are all obtained over a span of 40 mT, so as to contain a sufficient number of oscillations. Figure 6(*a*) uses data centered at $B = 0$ spanning -20 mT to 20 mT, (*b*) 20 mT to 60 mT, (*c*) 60 mT to 100 mT, (*d*) 100 mT to 140 mT and (*e*) 140 mT to 180 mT, at which B the AAS oscillations have decayed. It is noticeable that whereas the AAS oscillation amplitude decays with increasing center B, the MZ oscillations maintain approximately constant amplitude. Figures 4(*a*) and (*b*) also demonstrate that MZ oscillations survive essentially unaffected at higher B. Figure 7(*a*) depicts the AAS ($h/2e$) Fourier amplitude versus B as obtained from figure 6. The ordinate contains the height of the $h/2e$ Fourier component, while the abscissa corresponds to the center value of $|B|$ of the Fourier transform spans. The first datapoint thus lies at $B = 10$ mT and subsequent datapoints at 40 mT, 80 mT, 120 mT and 160 mT. Figure 7(*a*) clearly shows the decay of the AAS oscillation amplitude with increasing B. We note that oscillations periodic in $h/2e$ can in principle also occur as higher harmonics of MZ oscillations [19]. However, in ring arrays such MZ contribution will be small due to ensemble averaging. The observed decay with increasing B of the $h/2e$ component also strongly favors its identification as an AAS ST contribution. Using the same method, figure 7(*b*) depicts the height of the MZ (h/e) Fourier component versus B over a wider range of B, demonstrating that although the MZ oscillation amplitude varies due to local ϕ [19], no monotonic decay with increasing B is apparent. The differing behavior of the AAS and MZ oscillations originate in the different symmetries, respectively temporal and spatial, they are sensitive to.

The magnetic dephasing length $L_B(B)$ assumes different forms depending on the relative values of $l_m \equiv \sqrt{\hbar/(eB)}$, l_e and w. As mentioned, in an unconfined system without impediment to flux accumulation over a closed path and where necessarily $l_m \ll w$ and $l_e \ll w$, we have the unconfined diffusive expression for $L_B(B)$

$$L_B = l_m \tag{2}$$

Still in the diffusive regime ($l_e < w$) and with diffusive boundary scattering, yet in a narrow wire and at low B with $l_m > w$, such that boundary conditions at the wire edges modify the Landau level states, we have [25]

$$L_B = \sqrt{3} l_m^2 / w \tag{3}$$

In the diffusive regime but where $l_m \simeq w$, a crossover expression [32] can be applied,

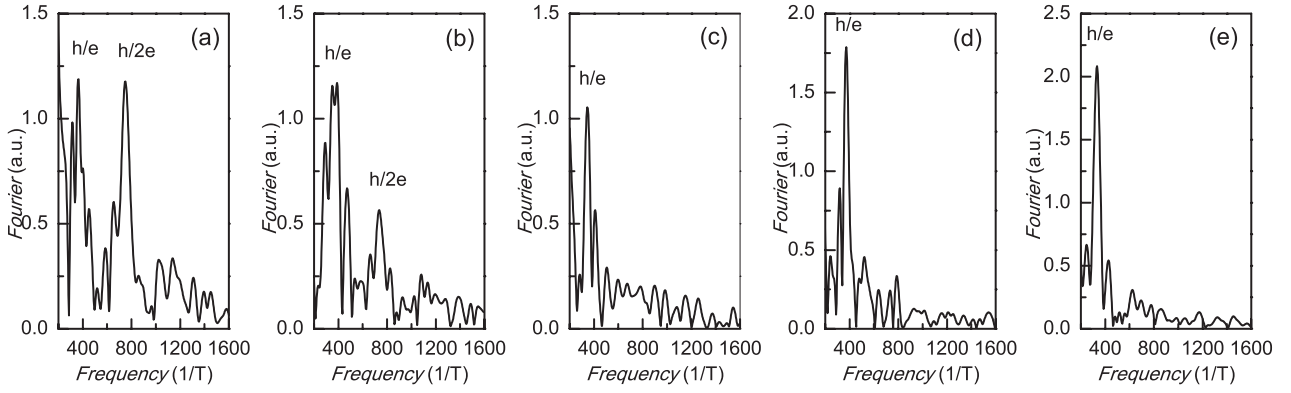$$L_B = \sqrt{l_m^2 + 3 l_m^4 / w^2} \tag{4}$$

Figure 6. Fourier spectra illustrating the decay of AAS ($h/2e$) oscillations and the survival of MZ (h/e) oscillations with increasing B. Fourier spectra use a 40 mT span, centered at 0 mT (*a*), 40 mT (*b*), 80 mT (*c*), 120 mT (*d*) and 160 mT (*e*).
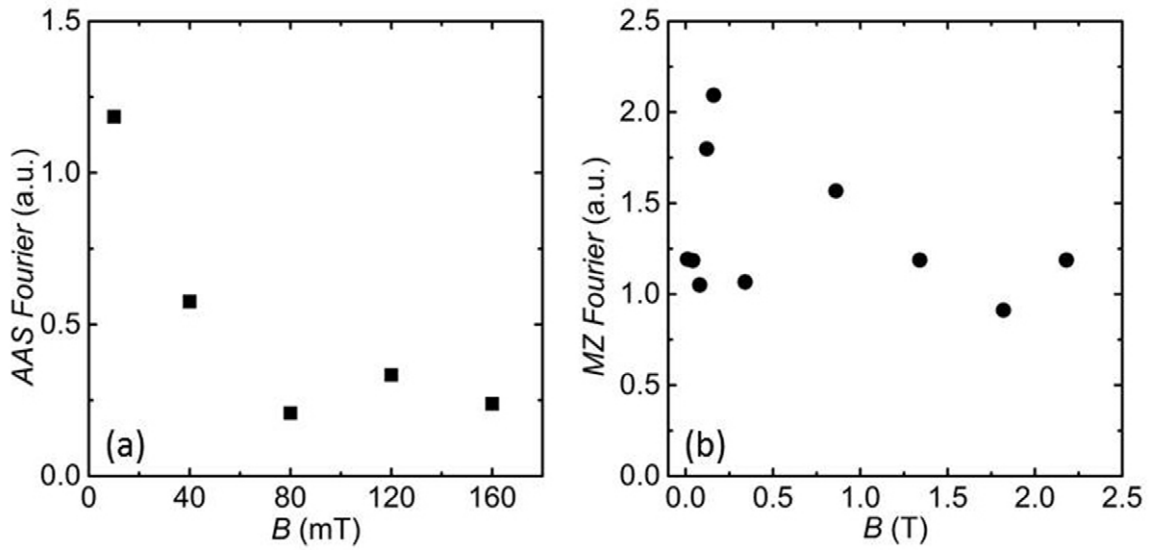

Figure 7. Fourier component amplitudes (arbitrary units) versus B (B-values determined as explained in the text). (*a*) AAS ($h/2e$) Fourier component versus B, illustrating the decay of AAS oscillations with increasing B. (*b*) MZ (h/e) Fourier component versus B, illustrating the lack of monotonic decay of MZ oscillations with increasing B.

In the ballistic regime where $l_e \geqslant w$ and at low B limited by $l_m > \sqrt{w l_e}$, we have an expression taking flux cancellation into account [27, 28]

$$L_B = l_m \sqrt{C_1 l_m^2 l_e / w^3} \qquad (5)$$

Still in the ballistic regime ($l_e \geqslant w$) and at intermediate B such that $w < l_m < \sqrt{w l_e}$, we have a crossover expression [27, 28]

$$L_B = l_m \sqrt{C_1 l_m^2 l_e / w^3 + C_2 l_e^2 / w^2} \qquad (6)$$

C_1 and C_2 are numerical constants with values depending on whether the boundary scattering at wire edges is specular or diffusive. Specular boundary scattering is expected in wires fabricated from the $In_{0.64}Ga_{0.36}As/In_{0.45}Al_{0.55}As$ heterostructure due to the presence of a depletion layer at the wire edge (for an example of diffusive boundary scattering, see [22]). For specular boundary scattering in a 2DES, $C_1 = 4.75$ and $C_2 = 2.4$ [28]. The ring array, with $w \simeq 100$ nm and $l_e = 1.54\,\mu$m, should satisfy the ballistic condition.

With knowledge of $L_B(B)$ and L_ϕ, equation (1) provides the effective coherence length $L_C(B)$. In order to determine which model (equations (2)–(6)) fits the experimental data best, we have to introduce a method to map the AAS oscillation amplitude to the coherence length L_C. For a quantum-coherent interferometer array, an expression more complex than an exponential decay with characteristic length L_C is appropriate [14]. From [15] we have isolated the oscillatory part of the resistance due quantum interference effects in transport through interferometer arrays and we find that the amplitude A of the AAS oscillations can be expressed as

$$A = \alpha (L_C/L)(1 - \tanh(L/L_C)) \qquad (7)$$

where α is a prefactor and $L = \pi r$. At low B, we can assume $L_B \gg L_\phi$, such that $L_C \approx L_\phi = 3\,\mu$m. We thus use the datapoint at the lowest $B = 10$ mT in figure 7(*a*) to calibrate α using $L_C = 3\,\mu$m in equation (7). For the remaining 4 field points, the value of $L_C(B)$ can then be obtained and hence the value of $L_B(B)$ experimentally determined using equation (1). The results are depicted in figure 8 as experimental data (the
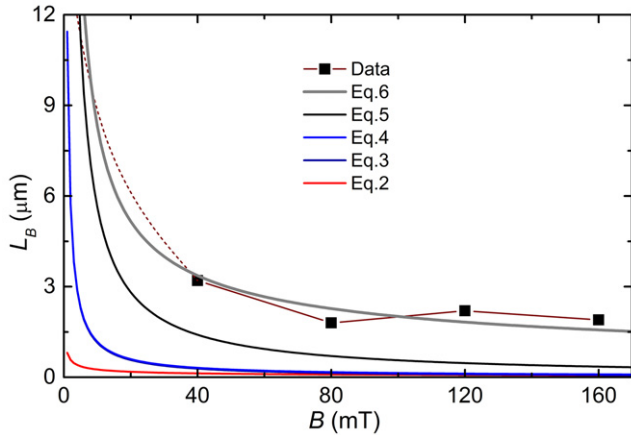
Figure 8. Experimental data for L_B (black squares) and calculated curves for L_B according to (bottom to top curves) equations (2)–(6) (curves for equations (3) and (4) mostly overlap for the present parameters and cannot be distinguished on the graph). The experimental data are extracted using figure 7(*a*) as explained in the text.

calibration point at $B = 10$ mT lies off the graph since for this datapoint L_B is assumed very long; a guideline was used to connect this point to the remaining data). Figure 8 also plots values of L_B calculated from equations (2)–(6). The model described by equation (6) provides the best match to the experimental values of L_B.

The result that the experimental data for $L_B(B)$ follows equation (6) is reasonable. The system is confined to a wire of width w and is in ballistic regime, with $l_e > w$. Hence equations (2)–(4) are not expected to be suitable and the data indeed bears out this observation. The condition $l_m > \sqrt{wl_e}$ for equation (5) implies that $B < 3.8$ mT. In figure 8, B exceeds 3.8 mT and hence equation (5) is not expected to fit the data except at the lowest B where no independent data is available. Using the condition $w < l_m < \sqrt{wl_e}$, we obtain 3.8 mT $< B < 66$ mT. The condition implies that equation (6) is expected to match the data in this range of B. The experiment bears out that in fact equation (6) provides a good description of $L_B(B)$ not only in this range, but beyond $B = 66$ mT. We also note that at the higher B, C_1 can be set to 0. However, since our data was obtained from -20 mT to 180 mT, a range that includes low B, the full crossover expression given by equation (6) provides a prediction for $L_B(B)$ valid over a wide range of B in our ballistic system.

A single ring in the array has a circumference $\approx 4\,\mu$m. We can thus expect that when L_B is smaller than this value, the AAS oscillation amplitude should decrease significantly. The data in figure 8 is consistent with this expectation, as the Fourier transform height of the AAS oscillations almost merges into the background for $L_B \leqslant 3\,\mu$m. We note that an increase in AAS oscillation amplitude can be achieved by excluding the local ϕ from the interferometer arms, although an experimental realization of this approach will prove challenging. Alternatively, narrowing w will yield a more practical avenue to increase the AAS oscillation amplitude, as in equations (3)–(6) L_B will lengthen with narrowing w. Insight in this relation follows from considering

that if a closed path is constrained to w along a transverse direction in a wire, acquiring a given AB phase will require that the partial wave travel over $\sim l_m^2/w$ in the longitudinal direction, which becomes the effective free length for AB phase accumulation, or hence the effective magnetic length and time-reversal symmetry breaking length. The lengthening of L_B with narrowing w hence has a geometrical origin, in a delay of accumulated local ϕ to higher B. The MZ oscillations are not similarly affected by the local ϕ, as the MZ interference does not rely on time-reversal symmetry and hence remains unaffected by L_B.

4. Conclusions

The mesoscopic dephasing length scale describing time-reversal symmetry breaking due to local magnetic flux was measured using a ballistic interferometer array, fabricated on a two-dimensional electron system in an InGaAs/InAlAs heterostructure. The interferometer array showed both Mach–Zehnder operation, yielding a magnetoresistance with flux periodicity of h/e and Sagnac-type operation based on time-reversed paths, yielding a periodicity of $h/2e$ (Altshuler–Aronov–Spivak oscillations). Fourier transforms over short magnetic field segments were used to quantify the oscillation amplitudes, confirming that the Mach–Zehnder mode of operation is unaffected by time-reversal symmetry breaking under an applied magnetic field, whereas Sagnac-type operation is erased by time-reversal symmetry breaking. Amplitudes were compared to predictions for $h/2e$ oscillations in quantum-coherent interferometer arrays, allowing experimental determination of the dephasing lengths associated with time-reversal symmetry breaking, equivalent to effective magnetic lengths. An analytical expression for effective magnetic lengths in confined ballistic systems yielded the best fit to experimental values.

References

[1] Aharonov Y and Bohm D 1959 *Phys. Rev.* **115** 485
[2] Washburn S and Webb R A 1986 *Adv. Phys.* **35** 375
[3] Oliaru S and Popescu I I 1985 *Rev. Mod. Phys.* **57** 339
[4] Aronov A G and Yu V S 1987 *Rev. Mod. Phys.* **59** 755
[5] Buttiker M 1986 *Phys. Rev. Lett.* **57** 1761
[6] Benoit A D *et al* 1986 *Phys. Rev. Lett.* **57** 1765
[7] Schopfer F *et al* 2007 *Phys. Rev. Lett.* **98** 026807
[8] Ferrier M *et al* 2004 *Phys. Rev. Lett.* **93** 246804
[9] Ludwig T and Mirlin A D 2004 *Phys. Rev. B* **69** 193306
[10] Meijer F E *et al* 2004 *Phys. Rev. B* **69** 035308
[11] Stone D A and Imry Y 1986 *Phys. Rev. Lett.* **56** 189
[12] Umbach C P *et al* 1986 *Phys. Rev. Lett.* **56** 386

[13] Lillianfeld R B *et al* 2010 *Phys. Procedia* **3** 1231
[14] Doucot B and Rammal R 1985 *Phys. Rev. Lett.* **55** 1148
[15] Dolan G J *et al* 1986 *Phys. Rev. Lett.* **56** 1493
[16] Ferrier M *et al* 2008 *Phys. Rev. Lett.* **100** 146802
[17] Texier C *et al* 2009 *Phys. Rev.* B **80** 205413
[18] Treiber M *et al* 2009 *Phys. Rev.* B **80** 201305
[19] Ren S L *et al* 2013 *J. Phys.: Condens. Matter* **25** 435301
[20] Altshuler B L *et al* 1984 *Sov. Phys.—JEPT* **59** 415 (Engl. transl.)
     Altshuler B L *et al* 1984 *Zh. Eksp. Teor. Fiz.* **86** 709
[21] Lin J J and Bird J 2002 *J. Phys.: Condens. Matter* **14** R501
[22] Kallaher R L *et al* 2013 *Phys. Rev.* B **88** 205407
[23] Hackens B *et al* 2005 *Phys. Rev. Lett.* **94** 146802
[24] Akkermans Eric and Montambaux Gilles 2007 *Mesoscopic Physics of Electrons and Photons* (Cambridge: Cambridge University Press)
[25] Altshuler B L and Aronov A G 1981 *J. Exp. Theor. Phys.* **33** 499 (Engl. transl.)
     Altshuler B L and Aronov A G 1981 *Pis'ma Zh. Eksp. Teor. Fiz.* **33** 515
[26] Bergmann G 1984 *Phys. Rep.* **207** 1
[27] Dugaev V K and Khmelnitskii D E 1984 *Sov. Phys.—JEPT* **59** 1038 (Engl. transl.)
     Dugaev V K and Khmelnitskii D E 1984 *Zh. Eksp. Teor. Fiz.* **86** 1784
[28] Beenakker C W J and van Houten H 1988 *Phys. Rev.* B **38** 3232
[29] Hikami S *et al* 1980 *Prog. Theor. Phys.* **63** 707
[30] Iordanskii S V *et al* 1994 *JEPT Lett.* **60** 206 (Engl. transl.)
     Iordanskii S V *et al* 1994 *Pis'ma Zh. Eksp. Teor. Fiz.* **60** 199
[31] Heremans J J *et al* 2014 *Proc. SPIE* **9167** 91670D
[32] Kettemann S 2007 *Phys. Rev. Lett.* **98** 176808